

SIMULTANEOUS *CHANDRA* AND *RXTE* SPECTROSCOPY OF THE MICROQUASAR H 1743–322: CLUES TO DISK WIND AND JET FORMATION FROM A VARIABLE IONIZED OUTFLOW

J. M. MILLER^{1,2}, J. RAYMOND¹, J. HOMAN³, A. C. FABIAN⁴, D. STEEGHS¹, R. WIJNANDS⁵, M. RUPEN⁶, P. CHARLES⁷,
 M. VAN DER KLIS⁵, W. H. G. LEWIN³,

Subject headings: Black hole physics – relativity – stars: binaries (H 1743–322) – stars: binaries – physical data
 and processes: accretion disks

Draft version March 20, 2018

ABSTRACT

We observed the bright phase of the 2003 outburst of the Galactic black hole candidate H 1743–322 in X-rays simultaneously with *Chandra* and *RXTE* on four occasions. The *Chandra*/HETGS spectra reveal narrow, variable (He-like) Fe XXV and (H-like) Fe XXVI resonance absorption lines. In the first observation, the Fe XXVI line has a FWHM of 1800 ± 400 km/s and a blue-shift of 700 ± 200 km/s, suggesting that the highly ionized medium is an outflow. Moreover, the Fe XXV line is observed to vary significantly on a timescale of a few hundred seconds in the first observation, which corresponds to the Keplerian orbital period at approximately $10^4 r_g$ (where $r_g = GM/c^2$). Our models for the absorption geometry suggest that a combination of geometric effects and changing ionizing flux are required to account for the large changes in line flux observed between observations, and that the absorption likely occurs at a radius less than $10^4 r_g$ for a $10 M_\odot$ black hole. Viable models for the absorption geometry include cyclic absorption due to an accretion disk structure, absorption in a clumpy outflowing disk wind, or possibly a combination of these two. If the wind in H 1743–322 has unity filling factor, the highest implied mass outflow rate is 20% of the Eddington mass accretion rate. This wind may be a hot precursor to the Seyfert-like, outflowing “warm absorber” geometries recently found in the Galactic black holes GX 339-4 and XTE J1650–500. We discuss these findings in the context of ionized Fe absorption lines found in the spectra of other Galactic sources, and connections to warm absorbers, winds, and jets in other accreting systems.

1. INTRODUCTION

The Galactic X-ray transient H 1743–322 was classified as a black hole candidate by White & Marshall (1984) based on its X-ray spectral characteristics. The source was discovered during its 1977–1978 outburst with *HEAO-1* and *Ariel V* (Doxsey et al. 1977, Kaluzienski & Holt 1977). The next convincing detection of H 1743–322 was made on 2003 March 21 with *INTEGRAL* (Revnivtsev et al. 2003) and later with *RXTE* (Markwardt & Swank 2003a), earning the source the additional designations IGR J17464–3213 and XTE J1746–322. Markwardt & Swank (2003b) pointed out that although the original *HEAO-1* detection reported two possible locations, it was very likely that the potentially new transient was actually H 1743–322. Following its 2003 re-activation in X-rays, the source was extensively monitored in optical, IR, and radio bands (see, e.g., Rupen, Mioduszewski, & Dhawan 2003; Steeghs et al. 2003 and ref. therein).

Two discoveries made during the 2003 outburst of H 1743–322 have provided additional evidence that this source harbors a black hole primary. First, Homan et al. (2003) reported the detection of quasi-periodic oscillations (QPOs) at 240 Hz in the *RXTE* X-ray flux. This frequency is typical of black hole candidates, and is tantalizingly close to

the Keplerian orbital frequency expected at the innermost stable circular orbit (ISCO) around a Schwarzschild black hole ($\nu \simeq 220$ Hz ($10 M_\odot/M_{BH}$)). Moreover, there is evidence for QPOs at 160 Hz, and therefore in the 2:3 ratio which has recently emerged in a few Galactic black hole systems (GRO J1655–40: Strohmayer 2001a, GRS 1915+105: Strohmayer 2001b, XTE J1550–564: Miller et al. 2001, and possibly XTE J1650–500: Homan et al. 2003b). The apparent 2:3 pairing may be evidence of a parametric epicyclic resonance in black hole accretion disks (see, e.g., Abramowicz & Kluzniak 2003). However, there is evidence that black hole QPO pairs may drift out of a 2:3 ratio (Miller et al. 2001, Remillard et al. 2002), and the 2:3 ratio described by the resonance model for so-called kHz QPOs in neutron star systems is at odds with data (Miller 2003).

Second, radio observations have revealed a jet in H 1743–322, moving at $v/c \simeq 0.8$ (Rupen, Mioduszewski, & Dhawan 2004). On the basis of this relativistic jet, H 1743–322 may be termed a “microquasar”. Indeed, the X-ray spectroscopic results presented in this paper will further establish close similarities between H 1743–322 and microquasars like GRO J1655–40 and GRS 1915+105, in addition to their radio jet and X-ray timing similarities. Although highly relativistic

¹Harvard-Smithsonian Center for Astrophysics, 60 Garden Street, Cambridge, MA 02138, jmmiller@cfa.harvard.edu

²NSF Astronomy and Astrophysics Fellow

³Center for Space Research and Department of Physics, Massachusetts Institute of Technology, Cambridge, MA 02139–4307

⁴Institute of Astronomy, University of Cambridge, Madingley Road, Cambridge CB3 0HA, UK

⁵Astronomical Institute “Anton Pannekoek,” University of Amsterdam, and Center for High Energy Astrophysics, Kruislaan 403, 1098 SJ, Amsterdam, NL

⁶National Radio Astronomy Observatory, Array Operations Center, 1003 Lopezville Road, Socorro, NM 87801

⁷Department of Physics and Astronomy, University of Southampton, SO17 1BJ, England, UK

jets are not a unique black hole primary signature (Fender et al. 2004), such jets are more commonly observed in black hole systems than in neutron star systems.

We observed H 1743–322 simultaneously with *Chandra* and *RXTE* on four occasions during the bright phase of its 2003 outburst, as part of our larger multi-wavelength black hole observing program. Herein, we report the results of an analysis of the X-ray spectra resulting from these observations. Most importantly, the *Chandra*/HETGS spectra reveal variable He-like Fe XXV and H-like Fe XXVI resonance absorption lines, which may be due to absorption in an outflow. Variable, Seyfert-like “warm-absorber” outflows have recently been detected in the X-ray spectra of the Galactic black holes XTE J1650–500 and GX 339–4 (Miller et al. 2004a, Miller et al. 2004b). We examine the absorption in H 1743–322 within the context of these recent results. The results of an analysis of the X-ray timing properties of the *RXTE* observations will be reported in a companion paper (Homan et al. 2004). The results of radio observations made in partial support of this program will be reported in a separate paper by Rupen et al. (2004, in prep.), and results from optical and IR observations will be reported in Steeghs et al. (2004, in prep.).

2. OBSERVATION AND DATA REDUCTION

We observed H 1743–322 with *Chandra* and *RXTE* on four occasions during the bright phase of its 2003 outburst, as part of ongoing and complementary Target of Opportunity programs to study Galactic black holes in outburst in X-rays. The *Chandra* observations were each approximately 50 ksec in duration. *RXTE* made observations simultaneous with each of these *Chandra* observations, with individual exposure times ranging between 0.6 ksec and 25 ksec. The observation dates, starting times, and net exposure times are given in Table 1.

2.1. *RXTE* Spectral Reduction

At the time of writing, PCU-2 is the best-calibrated PCU in the *RXTE*/PCA, based on simple power-law fits to the Crab spectrum. In order to best search for subtle features like broad Fe K α lines, we restricted our PCA spectral reduction and analysis to PCU-2. Spectra from the HEXTE-A cluster were included for spectral reduction and analysis to constrain the high energy continuum. *RXTE* data reduction tools in the HEASOFT version 5.2 suite were used to screen the event and spectral files.

Spectra from PCU-2 were extracted from data taken in “Standard 2” mode, providing full coverage of the 2.0–60.0 keV PCA bandpass in 129 channels every 16 seconds. Data from all of the Xe gas layers in PCU-2 was combined. Background spectra were made using the tool “pcabackest” using the latest “bright source” background model. Redistribution matrix files (rmfs) and ancillary response files (arfs) were made and combined into a single file using the tool “pcarsp.” The background spectra were subtracted from the total spectrum using the tool “mathpha.” It is well-known that fits to PCA spectra of the Crab with a simple power-law model reveal residuals as large as 1%, but adding 1% systematic errors to PCA data is often an overestimate. Using the tool “grppha”, we added 0.6% systematic errors to the spectra from PCU-2. The lowest energy bins in the PCA are poorly calibrated, and the calibration above 25 keV is uncertain; we therefore restricted our PCU-2 spectral analysis to the 3–25 keV range.

The HEXTE-A spectra were made from standard “archive” mode data, which has a nominal time resolution of 32 s and covers the 10–250 keV range with 61 channels. All spectra

were background-subtracted and deadtime corrected using the standard procedures. The calibration of the energy channels below 20 keV is poor, and we therefore restricted our analysis of the HEXTE spectra to energies above 20 keV. As some of the spectra are soft and therefore dominated by background above 100 keV, we fixed this energy as an upper bound for consistency. However, analysis of the spectra up to 250 keV was undertaken for those spectra with sufficient signal.

The *RXTE* spectra were analyzed using XSPEC version 11.2.0 (Arnaud & Dorman 2000). All errors on fits to the *RXTE* spectra are 90% confidence errors.

2.2. *Chandra* Spectral Reduction

In each *Chandra* observation, the High Energy Transmission Grating Spectrometer (HETGS) was used to disperse the incident flux onto the ACIS-S CCD array. The ACIS-S array was read-out in “continuous-clocking” mode (nominal frametime: 2.8 msec) to prevent photon pile-up. Information is collapsed into one dimension to achieve the fast read-out in this mode; thus, our *Chandra* observations were purely spectroscopic as imaging information was not preserved. A 100-column “gray filter” window was used around the aimpoint on the ACIS-S3 chip, which acted to read-out only one in every ten zeroth-order events. This step was taken to prevent telemetry saturation and frame drop-out on the S3 chip. We shifted the location of the aimpoint from the nominal S3 aimpoint. A Y-coordinate offset of 0.33 arcmin was used to shift the wavelength at which CCD chip gaps occur in order to ensure a simple response function in the Fe K line region, and a SIM-Z offset of –7.5 mm was used to push the aimpoint toward the CCD read-out to limit charge transfer inefficiencies and to limit wear and tear on the prime imaging area of the S3 chip.

Spectra and lightcurves were extracted from the *Chandra* event lists using the CIAO version 2.3 reduction and analysis suite. The “evt1” file was filtered to accept only the standard event grades, to accept only events from the nominal good time intervals, and to exclude bad pixels. The “de-streak” tool was run to remove the effects of “streaking” in the CCDs. Although imaging information is not preserved in the mode used for these observations, the CIAO HETGS spectral extraction routines are robust for locating the observation aimpoint, defining a wavelength grid, and extracting spectra. Spectra were extracted using the default settings for the tools “tg_resolve_events” and “tgextract.” We used the canned redistribution matrix files (rmfs) to make ancillary response files (arfs) via the “fullgarf” tool. The first-order HEG spectra and arfs were added to make a single spectrum and single arf using the tool “add_grating_spectra”; the same addition was done with the first-order MEG spectra. In the analysis detailed below, we only claim spectral features which are readily detected in the individual dispersed spectra (prior to addition).

The *Chandra*/HETGS spectra were fit with ISIS version 1.1.3 (Houck & Denicola 2000). All errors on the absorption line parameters measured from the HETGS spectra are 1σ errors.

In this paper, we have restricted our analysis to the first-order HEG spectra. Moreover, we fit only phenomenological power-law continua and simple Gaussian line functions in a range spanning less than 1 Å. The primary reasons for these restrictions are (1) the low-energy portions of the MEG and HEG spectra do not reveal any evidence for narrow emission or absorption lines, and (2) only the HEG spectra have sufficient sen-

sitivity through the Fe K line range to allow meaningful analysis and constraints.

For the benefit of scientists examining these spectra in the future, we note some additional reasons behind the above restrictions, since they are related to nuances of the telescope and the observing mode employed. H 1743–322 had a flux roughly equivalent to or greater than 1 Crab in the *RXTE*/ASM (1.5–12.0 keV) during the first *Chandra* observations, despite the high column density along the line of sight to this source. When fit with the spectral shapes that describe the *RXTE* spectra well, the *Chandra*/HETGS spectra show positive residuals above approximately 8 keV, and also at energies below approximately 2 keV. These effects are inconsistent with photon pile-up, and inconsistent with the effects expected due to contaminant build-up on the ACIS chips. Rather, the positive residuals above ~ 8 keV are likely due to incident photons scattering off the instrument support structure and falling into the high energy portion of the dispersed spectra (which is closest to the zeroth order). The nature of the positive residuals below ~ 2 keV is less certain. If the standard CIAO tools over-correct for charge transfer inefficiency at our offset, such a correction might partially account for the positive residuals.

While these problems do not affect our ability to search for narrow emission and absorption lines through the full HETGS bandpass, we were unable to fit the full HETGS continuum with meaningful models, and we do not report such fits in this work. We note, however, that in the 2.5–7.5 keV range, the *Chandra*/HETGS spectra broadly agree with the *RXTE* spectra. The positive residuals above ~ 8 keV made it impossible to measure the depth of the (He-like) Fe XXV and (H-like) Fe XXVI K edges at 8.8 keV and 9.3 keV (respectively). Balancing the optical depth of these K-shell absorption edges with the optical depth of the Fe XXV and Fe XXVI absorption lines we detected (see below) would have allowed tighter constraints. Nevertheless, a number of important constraints can be made using only the variable Fe XXV and Fe XXVI absorption lines detected in these spectra, and we report measurements of the line parameters, a model for the absorption, and implications for the accretion inflow and outflow in H 1743–322 in this work.

3. ANALYSIS AND RESULTS

3.1. Broad-Band Spectral Fits

We made fits to each of the time-averaged *RXTE* spectra listed in Table 1 with simple, phenomenological spectral models. Initial fits revealed that an equivalent neutral hydrogen column density of $N_H = 2.3 \times 10^{22} \text{ cm}^{-2}$ was easily within the error bars of each individual measurement. Therefore, we fixed this value in all subsequent fits. This column is higher than that predicted from radio measurements ($N_H \simeq 7 \times 10^{21} \text{ cm}^{-2}$, Dickey & Lockman 1990); however, the radio estimates are limited by the coarse spatial resolution of the survey observations. Our spectral model consisted of the multicolor disk blackbody (MCD; Mitsuda et al. 1984) and power-law components. As the name implies, the MCD model is included to account for soft, thermal, blackbody-like emission thought to arise from an optically-thick but geometrically-thin accretion disk. The power-law component is likely primarily the result of Compton-upscattering of disk photons by a central, hot, electron-dominated “corona”. This region may not be distinct from the base of a jet; if it is distinct, processes like synchrotron self-Compton emission from the base of a jet may also contribute to the hard power-law component.

The results of spectral fits in the 3–100 keV band with this absorbed MCD plus power-law are reported in Table 2, and an example spectral fit is shown in Figure 1. The spectral parameters obtained through our fits are typical of Galactic black hole candidates in bright phases. In general, statistically acceptable fits are obtained ($\chi^2/\nu \simeq 1$, where ν is the number of degrees of freedom in the fit) with this simple model. (The fits would be statistically improved if the Xe edge at approximately 4.8 keV was better described in the detector response.) The disk temperature varies between $kT = 1.0 - 1.2$ keV in our observations, indicating that the disk is likely important throughout the bright phase of the outburst and close to the innermost stable circular orbit (ISCO). The broad-band spectral properties indicate that H 1743–322 was likely in an extended “very high” or “steep power-law” state in observations 1a, 1b, 1c, 2a, 2b, 2c. Observation 3 occurred in a phase intermediate between the “high/soft” and “very high” (“steep power law”) state, but was likely more similar to the “high/soft” (or, “thermal-dominant”) state. Observations 4a, 4b, and 4c likely occurred in the “high/soft” (or, “thermal-dominant”) state. The states observed in H 1743–322 differ in subtle ways from canonical black hole states, however, and the reader is referred to Homan et al. 2004 (in prep.) for a more complete analysis and discussion of the states observed.

The highest flux inferred in the 0.5–10.0 keV band is $7.8 \pm 0.8 \times 10^{-8} \text{ erg cm}^{-2} \text{ s}^{-1}$, which corresponds to a luminosity of $L_X = 6.8 \pm 0.7 \times 10^{38} (d/8.5 \text{ kpc})^2 \text{ erg s}^{-1}$ (see Table 2). At present, neither the mass of H 1743–322 nor the distance to the source are known. Given its Galactic center position and rather high column density, however, it is reasonable to use a Galactic center distance of 8.5 kpc as an estimate of the distance to the source. At such a distance, the source emission was (just) sub-Eddington for a $6 M_\odot$ black hole (and more comfortably sub-Eddington for a $10 M_\odot$ black hole).

Since Homan et al. (2003a) detected QPOs at 240 Hz and 160 Hz in H 1743–322, which may be indicative of black hole spin as the QPOs are in a 2:3 ratio (Abramowicz & Kluzniak 2003), it is worth addressing whether or not our spectral fits support the inference of a disk extending very close to a potentially spinning black hole. The MCD model allows a measure of the inner disk radius through its normalization: $K = [(r_{in}/\text{km})/(d/10 \text{ kpc})]^2 \times \cos(\theta)$ (where θ is the inclination of the disk to the line of sight). The smallest disk normalization is measured in observation 2b. Via the normalization, $r_{in} \simeq 30 \text{ km}$ for $d = 8.5 \text{ kpc}$ and $\theta = 45^\circ$, and $r_{in} \simeq 50 \text{ km}$ for $d = 8.5 \text{ kpc}$ and $\theta = 80^\circ$. The ISCO around a non-spinning black hole is $r_{ISCO} = 6 r_g$ (where $r_g = GM_{BH}/c^2$; $r_g \simeq 1.5 \text{ km} (M_{BH}/M_\odot)$). For black hole masses greater than $10 M_\odot$, $R_{in} \leq 90 \text{ km}$ may imply spin and support any such implications from the QPOs previously detected. However, this simple analysis has a few important problems and the inferred radii should be regarded cautiously. The MCD model does not include an inner boundary condition, and inclination effects and radiative processes in the disk can be important and have not been accounted for in this exercise (see, e.g., Shimura & Takahara 1995, and Merloni, Fabian, & Ross 2000). Moreover, disk continuum spectroscopy is particularly sensitive to the absorption model and to the model for the hard component. Finally, QPO frequencies may not be simple Keplerian frequencies.

The broad-band *RXTE* spectra are remarkable for what they do not show:

First, although we have only fitted the data up to 100 keV

(since the softer spectra have little flux above this energy), there is no evidence for a break in the power-law component in any of the spectra. Breaks may indicate the electron temperature of the putative corona. The absence of such an observed break in these spectra may indicate that the coronal electron temperature is generally very high ($kT \simeq 100$ keV, or greater). Observation 2b provides an illustrative case. This observed spectrum is reasonably hard and has a high S/N, with H 1743–322 clearly detected out to 250 keV without a break. Replacing the power-law component in our spectral model with the compTT Comp-tonization model (in which the coronal electron temperature is a variable, Titarchuk 1994), $kT_e \simeq 160$ keV is obtained. The model underestimates the hard flux above 100 keV and is statistically poor ($\chi^2/\nu = 136.4/76$), but indicates that the coronal temperature may be very hot indeed.

Second, the spectra are free of any features expected to arise from disk reflection (see Fig. 1). Hard X-ray irradiation of the (relatively) cool accretion disk by the corona is expected to produce a characteristic set of features: an Fe K α emission line, a corresponding Fe K edge, and a Compton-backscattering hump peaking between 20–30 keV. Disk reflection features are an extremely common, if not ubiquitous feature of broad-band Galactic black hole X-ray spectra. Yet, there is no evidence for any of these features in any of the broad-band *RXTE* spectra we obtained. In Table 2, the 95% confidence upper limits on the strength of narrow and broad Fe K α emission lines are given (FWHM= 0 keV and FWHM= 2 keV, as per the Doppler broadening expected at the inner disk around a Schwarzschild black hole). In most cases, the upper limits are stringent ($W_{K\alpha} \leq 15$ eV). For a disk at the ISCO, reflection from a neutral disk is expected to produce an emission line with an equivalent width of ~ 180 eV (George & Fabian 1991). Especially in bright, high accretion rate phases, the disks around Galactic black holes are likely to be ionized, and ionized disk reflection models predict line equivalent widths that are a few times higher than the neutral case (see, e.g., Ross, Fabian, & Young 1999).

We made broad-band reflection fits to observation 2b to further address the nature of the inner accretion flow geometry in H 1743–322. We replaced the simple power-law model with the “constant density ionized disk model” (CDID Ross, Fabian, & Young 1999; Ballantyne, Ross, & Fabian 2001). The CDID model is particularly well-suited to highly ionized reflection, and includes Fe K α line emission self-consistently. We “smeared” the CDID model by convolving it with the Laor relativistic emission line function (Laor 1991). The disk emissivity ($J(r) \propto r^{-q}$; $q = 3$ is expected for a standard disk), the inner disk radius r_{in} (in units of $r_g = GM/c^2$), and inclination parameters in the smearing function variables in the spectral model. In all cases where the reflection fraction $R = \Omega/2\pi$ was allowed to vary, values along these lines were measured: $\log(\xi) = 5.0–5.5$, $r_{in} \simeq 2 r_g$, $q \simeq 3$, $\theta = 70–85^\circ$, and $R = \Omega/2\pi \leq 0.02$ (95% confidence). Such fits were formally acceptable ($\chi^2/\nu \simeq 1.0$) though clearly not statistically required over the phenomenological MCD plus power-law model. In fits with $R = 0.25$ fixed, even for $q = 7$ (extreme smearing) the fit was not acceptable $\chi^2/\nu \geq 2.0$. Fits with higher values of R fixed were statistically much worse.

3.2. *RXTE* Variability Analysis

The *RXTE* variability analysis conducted in this work follows the methods and procedures detailed in Homan et al. (2004b).

The reader is directed to that work for a full discussion of the timing analysis presented here.

An example lightcurve showing strong QPO-like variability on the timescale of *few* $\times 100$ s is shown in Figure 2. A power density spectrum of *RXTE* observation 1a is shown in Figure 3; the variability seen in the lightcurve corresponds to the broad 4×10^{-3} Hz peak in the power density spectrum. It is clear that much of the power is concentrated in this feature. The term “QPO” is usually reserved for features with $Q \geq 2$ when fit with a Lorentzian (where $\nu_{max} = \nu_0(1 + 1/4Q^2)^{1/2}$). As $Q \simeq 0.5$ for the 4×10^{-3} Hz feature, it may not be termed a QPO. However, it is important to note that, like a QPO, its fractional rms increases with increasing energy (Homan et al. 2004b; see Figures 2 and 5).

3.3. *Chandra*/HETGS Spectral Analysis

We began by analyzing the combined first-order HEG and MEG time-averaged spectra from each observation in narrow 2Å slices, through the 1.2–25Å range. The continuum in each slice was fitted with a simple phenomenological power-law model. Where required, absorption edge(s) due to neutral (atomic) photoelectric absorption in the ISM were included and scaled to $N_H = 2.3 \times 10^{22}$ cm $^{-2}$ (see Table 2). Line features were fit with simple Gaussian models. Line identifications are based on the calculations and line lists tabulated by Verner, Verner, & Ferland (1996). Column density estimates were derived using the relation:

$$W_\lambda = \frac{\pi e^2}{m_e c^2} N_j \lambda^2 f_{ij} = 8.85 \times 10^{-13} N_j \lambda^2 f_{ij}$$

where N_j is the column density of a given species, f_{ij} is the oscillator strength, W_λ is the equivalent width of the line in cm units, and λ is the wavelength of the line in cm units (Spitzer 1978). In using this relation, we have assumed that the lines are optically thin and that we are on the linear part of the curve of growth.

In observations 1, 3, and 4, we clearly detect absorption lines which we identify as He-like Fe XXV $1s^2 - 1s2p$ ($\lambda = 1.850\text{\AA}$) and H-like Fe XXVI $1s - 2p$ ($\lambda = 1.780\text{\AA}$) resonance absorption lines. The line wavelengths, velocity shifts, line breadths, fluxes, equivalent widths, columns, and equivalent neutral hydrogen columns are listed in Table 3. The spectra are shown in Figure 4. There is no clear evidence for any narrow emission or absorption lines in the rest of the spectrum. There are some line-like features in the region of the neutral Si edge which might be He-like Si XIII and H-like Si XIV; however, these are more likely due to uncertainties in the instrument response in this region (the spectrum peaks in this region, and the CCDs contain Si).

We have measured significant variability in the line equivalent widths and other parameters between observations, which demands changing absorption and clearly ties the lines to a region close to (or within) H 1743–322. In observation 2, when the source flux was high and twice as spectrally hard as in the other observations, the Fe XXV and Fe XXVI lines are absent. In observation 1, the lines are significantly blue-shifted, suggesting that the absorbing matter was flowing into our line of sight. The Fe XXVI line in observation 3 is also slightly blue-shifted. In all other cases, the lines are consistent with no net shift. In observations 1 and 4, the Fe XXVI lines are resolved, and have velocity widths (FWHM) of 1800 ± 400 km/s and 1900 ± 500 km/s, respectively. The rest of the lines are not resolved and likely have smaller velocity widths.

We made lightcurves of the dispersed spectrum from each observation in the 0.5–10.0 keV band. The lightcurves are presented in Figure 5. Strong variability is present in all observations on the timescale of $\text{few} \times 100$ s, but particularly in the first and second observations. This variability is confirmed to also be present in the lightcurves of the simultaneous *RXTE* lightcurves of H 1743–322 (see Fig. 2 and Fig. 3). A 10–12% “dip” feature may be present in the third *Chandra* observation. A preliminary examination of other *RXTE* observations in the public archive revealed much stronger dipping activity typical of dipping black hole binaries viewed at high inclinations (see, e.g., Kuulkers et al. 1998).

To explore whether the absorption lines vary within the dip, we made spectra of observation 3 from before the dip and within the dip (see Figure 5), and fit the spectrum in the manner noted above. Again, the only lines apparent are the Fe XXV and Fe XXVI absorption lines found in the time-averaged spectrum. The results of fits to the spectrum prior to the dip and within the dip are given in Table 4, and the spectra are shown in Figure 6. Both absorption lines are stronger within the dip. While the statistical significance of the variability in the Fe XXVI line is marginal, the variability in the strength of the Fe XXV line is clearly significant. Indeed, in observation 3, the Fe XXV line is not clearly detected in the pre-dip spectrum.

Next, we investigated whether the absorption lines in observation 1, and 4 vary on the $\text{few} \times 100$ s flaring variability timescale. We calculated the mean count rate for observations 1, 2, and 4 (see Fig. 5), produced lists of time intervals for count rates above and below the mean rate, and extracted spectra from the time intervals above and below the mean rates. Those spectra were also fitted in the manner described above; the spectra are shown in Figure 6. As was the case with the time-averaged spectrum of observation 2, the count-rate selected spectra of observation 2 show no absorption lines. In observation 4, the strength of the lines does not vary significantly between the high rate and low rate spectra. In observation 1, however, the absorption lines are marginally stronger in the low rate spectra than in the high rate spectra. This raises the interesting possibility that the absorption may vary on a timescale of $\text{few} \times 100$ s. To establish this more clearly, we created a list of time intervals in which the source count rate was more than 5 counts/s above the mean rate, and more than 5 counts/s below the mean rate, and extracted spectra from these time intervals. The resultant spectra are shown in Figure 7. The Fe XXV absorption line is clearly stronger in the low count rate spectrum than in the high count rate spectrum, and the variation is statistically significant (see Table 4).

3.4. Photoionized Plasma Models

To interpret the iron absorption lines measured in the time-averaged spectra in more detail, we computed line profiles from a spherical wind with a photoionization code. We used the atomic physics packages from the X-ray illuminated accretion disk models of Raymond (1993). In this case, since the gas is optically thin, it is only necessary to consider a single slab. We used the spectral parameters taken from Table 5 for each of the 4 observations and specify a density, slab thickness and distance from the central object, to model a 1-d, optically-thin wind. The code iterates to find a self-consistent temperature and ionization state, then computes equivalent widths assuming a Doppler profile with widths ranging from 100 to 2000 km s^{−1}. It assumes ionization equilibrium, which is a good approximation for the densities and dynamical times estimated below in

all cases. From the output of the code we find the parameters that match the observed Fe XXV and Fe XXVI absorption line equivalent widths.

The Fe XXV and Fe XXVI lines cannot originate in exactly the same gas, because the line widths and line shifts differ. A plausible physical picture might consist of denser, slower clumps containing more Fe XXV embedded in a less dense gas where Fe XXVI dominates. However, a modest density contrast of order 2 (approximately) is sufficient to shift the balance between Fe XXV and Fe XXVI, so an average density that produces both lines is meaningful, and we do not have enough measured parameters to justify the additional free parameters of a more complex model (the line widths are uncertain). We therefore choose densities to match the observed equivalent widths and Doppler velocity widths intermediate between those of Fe XXV and Fe XXVI.

There is a maximum radius at which a slab can plausibly be causing the observed absorption. The Fe XXVI/XXV line flux ratio gives an ionization parameter ($\xi = L_X/nr^2$), and for any given distance from the central source r , a specific density n is required. A specific slab thickness, which cannot exceed r , is required to produce the measured line column densities, so that $N \leq nr$. Because the density that gives the ionization parameter scales as r^{-2} , the slab thickness scales as r^{-2} (therefore $N \propto r^{-1}$), and there is a maximum radius at which a slab of thickness r can reproduce the lines observed. We call this parameter r_{max} . The lines can be formed at smaller r , and if the lines are formed in a wind with r^{-2} density profile, the density at r_{max} is correspondingly smaller.

Table 5 shows the derived parameters. We can also compute the mass loss rate in a wind of any velocity, because nr^{-2} is constant. The velocity shifts in Table 3 are generally uncertain, so we present mass loss rates for a reference wind speed of 300 km s^{−1}.

The table shows that the lack of absorption lines in the second observation cannot entirely be attributed to a higher ionizing flux. Although the ionizing flux in this observation is about double that of the first observation, an order of magnitude lower column density of absorbing material is needed to match the upper limits to the equivalent widths.

An interesting result in Table 5 is the small value of r_{max} for the 4th observation, which results primarily from the small ionizing flux. The lines do not show a significant Doppler shift, but they arise in a white dwarf-size region near the central source. In the first and third observations, the absorbing regions have a size comparable to a few solar radii, which is similar to the separation of the components in several binary black hole systems.

The second interesting aspect of the table is the indication that the observed absorption lines are formed in a wind with a mass loss rate of order $2 \times 10^{-8} M_\odot \text{ yr}^{-1}$ — comparable to the inferred mass accretion rate. If we assume a distance of 8.5 kpc, take the highest inferred 0.5–10.0 keV luminosity of $L_X = 6.8 \times 10^{38} \text{ erg s}^{-1}$ and assume an efficiency of 10% in the equation $L_X = \eta \dot{m}_{\text{acc}} c^2$, we obtain $\dot{m}_{\text{acc}} = 7.6 \times 10^{18} \text{ g s}^{-1}$. Taking the highest measured 0.5–10.0 keV luminosity to be a lower limit on the true Eddington luminosity, the highest inferred mass loss in the wind ($\dot{m}_{\text{wind}} = 1.7 \times 10^{18} \text{ g s}^{-1}$) corresponds to an outflow rate that is 22% of the Eddington mass accretion rate (for a unity filling factor). Note, however, that the fraction depends crucially on the filling factor, the energy range used, and the distance assumed. An outflow of this kind may be analogous to the accretion disk winds from cataclysmic

variables in their high states and to T Tauri stars in high states (FU Ori stars), which have wind mass loss rates of order 10% of their accretion rates. However, Observation 4 shows a much smaller mass loss rate along with its lower luminosity.

4. DISCUSSION

4.1. Geometric Constraints from the Broad-Band Spectral Fits

The high equivalent neutral hydrogen column density along the line of sight is consistent with a central Galactic distance to H 1743–322. For distances greater than $\simeq 3$ kpc, the highest 0.5–10.0 keV unabsorbed flux observed (see Table 2) exceeds the Eddington limit for a neutron star. Moreover, the parameters obtained from broad-band spectral fits to H 1743–322 with the phenomenological MCD plus power-law model are typical for Galactic black hole systems in bright phases (for a review, see McClintock & Remillard 2003, see also Homan et al. 2001). These facts — and the presence of 240 Hz QPOs in H 1743–322 — make it a near certainty that H 1743–322 harbors a black hole primary. However, the apparent absence of reflection features in the spectrum, even in phases with 1) a strong hard component, 2) a small inferred inner disk radius, and 3) high-frequency QPOs, is at odds with the majority of Galactic black holes.

It is likely that the low reflection fraction obtained is due to a combination of astrophysical effects (ionization and disk inclination) and the limitations of our reflection modeling. Zdziarski et al. (2003) have shown that when the disk is fully ionized, the reflected spectrum is nearly featureless, and might therefore be confused with a zero-reflection scenario. High disk ionization tends to smooth-out reflection features; the dips we have detected in the lightcurve of *Chandra* observation 3 and in additional public *RXTE* observations of H 1743–322 point to a system viewed at high inclination. At high inclinations, Doppler shifts become very important, and tend to smear-out reflection features. The CDID reflection model we fit to *RXTE* observation 2b indicates that the disk in H 1743–322 is likely highly ionized and seen at a high inclination. While these constraints are likely robust, it must be acknowledged that even the CDID model has limitations. It is implemented into XSPEC as a library of angle-averaged spectra. Finally, we note that if any reflection spectrum also passes through the hard X-ray emitting corona, which is likely if a corona hugs a disc viewed at high inclination, then the reflection component will be Comptonized and much less detectable (Petrucci et al 2001). It is possible, then, that the total reflection model — the CDID model smeared with a line function (for which inclination is a fit parameter) — does not address high inclinations correctly. Were the combination of ionization and inclination effects more accurately described by our model, it is likely that a high reflection fraction would have been within errors.

The best interpretation of our broad-band spectral fits, then, is that H 1743–322 is a black hole system seen at high inclination, with a very highly or completely ionized inner disk.

4.2. On the Nature of the Ionized Absorber

We have clearly detected variable, narrow Fe XXV and Fe XXVI resonance absorption lines in the spectra of H 1743–322. In the recent past, similar absorption lines have been detected in the microquasars GRO J1655–40 (Ueda et al. 1998), and GRS 1915+105 (Kotani et al. 2000) with *ASCA*, and in GRS 1915+105 with *Chandra* (Lee et al. 2002). Unfortunately, each of these prior spectra suffered heavily from photon

pile-up. The extraordinary sensitivity of the H 1743–322 spectra has allowed us to improve upon previous implications based on Fe XXV/XXVI absorption lines in microquasars in two important ways: First, we have measured blue-shifts in the lines detected in observation 1, providing direct evidence that the highly ionized absorbing geometry may be an outflow (previously, outflows were only asserted). Second, we have resolved the lines in two cases, and in other cases the lines are likely narrower than the instrumental resolution. The FWHM of the lines is vital for constraining the nature of the absorption.

Viable descriptions of the absorption geometry in H 1743–322 must be able to account for a number of our key findings, including: (1) the blue-shifts observed in the first *Chandra* observation, (2) the large line flux changes observed between observations (in particular, the absence of absorption lines in the second *Chandra* observation), and the stronger absorption seen in the dip observed during the third *Chandra* observation, and (3) the absence of Fe emission lines in the spectra, (4) the variability of the absorption lines in observation 1 on a timescale of a few hundred seconds, and (5) the absorption must occur at a radius smaller than the maximum radius at which our photoionization models suggest the lines may be produced. Two geometries satisfy or partially satisfy most of these requirements: cyclic absorption in a disk structure resulting from the high inclination, and absorption in an (potentially clumpy) outflowing disk wind.

The absence of Fe emission lines in the *Chandra* and *RXTE* spectra suggests that the absorbing geometry is not spherical (else, emission line photons would have scattered into our line of sight). Indeed, modeling of the absorbers in GRO J1655–40 (Ueda et al. 2004) and GRS 1915+105 (Kotani et al. 2000) also suggested a cylindrical, perhaps pancake-like absorbing geometry. Absorption in a disk structure — perhaps a disk atmosphere — is consistent with this constraint. However, this picture relies on relatively large covering and filling factors. The lack of emission lines in the spectra is also consistent with the absorption occurring in relatively dense clumps in a disk wind, with large covering factors but small filling factors. A clumpy wind is particularly appealing when one considers that at high mass accretion rates (such as in the first *Chandra* observation), our models for the absorber indicate that the wind would already be optically-thick at approximately $300 r_g$. Yet, we clearly see continuum spectral components consistent with viewing the innermost flow without significant obscuration. Moreover, if QPOs are tied to Keplerian frequencies, the QPOs detected (Homan et al. 2004, in prep.) indicate that emission from the innermost flow is either seen directly or scattered into our line of sight. A significant fraction of the absorption needs to occur in clumps with a high covering factor but small filling factor to be consistent with the observed continuum spectral properties and variability properties.

The absence of absorption lines due to a combination of geometric effects and ionizing flux (as implied by our photoionization models) in the second *Chandra* observation is easily explained by the clumpy outflow model. Simply, a clump may not have intersected our line of sight to the central accretion observation within this observation. It is more difficult to explain the absence of absorption lines if the absorption occurs via cyclic absorption in a disk structure. The disk structure would have to be dampened or disappear in the second *Chandra* observation. However, the ionizing flux is higher in this observation, and it has been shown that irradiation can induce warps in accretion

disks (see, e.g., Maloney, Begelman, & Pringle 1996).

To explain the enhanced absorption line fluxes measured within the dip in the third *Chandra* observation, it is easy to envision a cool clump absorbing Fe XXV more strongly than the hotter surrounding wind. Alternatively, it is also possible that the dip observed is due to an unrelated geometric effect, and that the enhanced absorption line flux seen within the dip occurs because the wind along our line of sight is temporarily shielded and allowed to cool. If the absorption lines are instead due to absorption in a disk structure, a second warp or disk structure may need to be invoked to explain the dip itself.

The variability of the Fe XXV absorption line flux on timescales of a few hundred seconds in the first *Chandra* observation can be explained by both models. Indeed, this short timescale line variability is one of the most compelling arguments in favor of cyclic absorption in a disk structure. The period of the line variability broadly agrees with the Keplerian orbital period at $10^4 r_g$ for a $10 M_\odot$ black hole. If H 1743–322 harbors a black hole with $M \simeq 10 M_\odot$, then $10^4 r_g$ corresponds to $\simeq 1.5 \times 10^{10}$ cm, which is less than r_{\max} in observations 1 and 3 (see Table 5). However, the observed variability cannot be termed a QPO, and it is therefore less easily tied to a cyclic disk structure than if it qualified as a true QPO. If the absorption occurs in a disk structure, it would suggest that the variability itself is due to changes in the absorption in our line of sight. This is at odds with the fact that similar variability is observed in the absence of absorption lines in the second *Chandra* observation. If the variability were due to absorption, the variability should be more pronounced at low energies; in fact, the fractional rms of the peak at 4×10^{-3} Hz increases with higher energy (Homan et al. 2004b; see Figures 2 and 5). Although it is less exciting, absorption in a clumpy outflowing wind can likely account for the rapid line flux variability at least as well as cyclic absorption in a disk structure. Simply, the gas ionization and recombination timescale is much faster than the variability timescale observed. If the variability is not due to a disk structure, but rather just due to fluctuations in the intensity of the central engine, an absorbing clump may be able to rapidly respond to the changing flux.

Finally, the blue-shifts observed in the first *Chandra* observation are more easily explained through an outflowing disk wind, than by absorption in the disk. The modest blue-shifts of the lines are a small fraction of the speed of light, and similar to the blue-shifted lines observed in GX 339–4 and XTE J1650–500 (Miller et al. 2004a), which are consistent with a disk wind. If the absorption is instead due to a cyclic disk structure, it is rather hard to explain the blue-shifts without significant fine-tuning. If the structure were a warp, its motion should be tangential to our line of sight, not into our line of sight. Instead, the absorption might need to occur in a disk wind flowing outward along the disk, and further postulate that the wind density is modulated by a cyclic disk structure underlying the atmosphere. It has been shown that accretion disks may drive outflows with a significant component along the disk (see, e.g., Murray & Chiang 1997, Proga 2003).

On balance, absorption in an outflowing, clumpy wind appears to be the more compelling than absorption in a disk structure. Both possibilities require a degree of fine-tuning to satisfy the observational constraints. A combination of these simple models may also be a viable description of the absorption geometry.

4.3. Connections to Warm Absorber Geometries

The highly ionized outflow revealed in these *Chandra* observations of H 1743–322 is very likely connected to the variable, outflowing, Seyfert-like warm absorbers recently discovered in GX 339–4 and XTE J1650–500 (Miller et al. 2004a, Miller et al. 2004b). In those systems, the outflowing absorbers are consistent with disk winds or shell ejections. The absorbers in GX 339–4 and XTE J1650–500 are blue-shifted, and so clearly outflowing. In GX 339–4, He-like Ne IX, Mg XI, and O VII absorption lines were detected simultaneously with more strongly blue-shifted Ne II and Ne III lines, suggesting a “clumpy” outflow with regions of differing temperature and density. The Fe XXV and Fe XXVI lines in H 1743–322 also need to come from distinct regions, though the contrast needed is much less than for the wind observed in GX 339–4. The outflow observed in GX 339–4 was likely detected at a lower fraction of the Eddington mass accretion rate in that source; its lower ionization can therefore be attributed to a lower central source flux. Moreover, the outflow in GX 339–4 implied an order of magnitude lower mass outflow rate than the highest rate implied in H 1743–322 (perhaps as high as 22% of the Eddington inflow rate). The outflow in H 1743–322 may be clumpy, however, and have a low filling factor; in that case, the outflow rate in H 1743–322 could be lower by a factor of $10^1 - 10^2$, or more.

It is plausible that the outflow in H 1743–322 is a hot, high $\dot{m}_{\text{wind}}/\dot{m}_{\text{Edd}}$ precursor to the cooler, lower $\dot{m}_{\text{wind}}/\dot{m}_{\text{Edd}}$ outflows observed in GX 339–4 and XTE J1650–500 (Miller et al. 2004a, 2004b). The mass outflow rate in the fourth *Chandra* observation of H 1743–322 is far less than that in the first observation (see Table 5), further indicating an evolution along the lines we suggest here. The outflows in these black hole systems are likely disk winds, and resemble the warm absorbers revealed in some Seyfert galaxies (see, e.g., Reynolds 1997, Elvis 2000, Morales & Fabian 2002). Such absorption regions could be tied to rather equatorial disk outflows (Murray & Chiang 1997, Proga 2003), rather than to a highly collimated flow perpendicular to the disk. Focused studies of Galactic black hole winds in the future may enable us to learn about the evolution Seyfert warm absorbers; their evolution is difficult to study directly given the inherently longer timescales.

4.4. On Possible Connections Between Ionized Absorption and Jets

It is worth addressing the possibility that a putative disk structure and the outflow are not merely coincident, but potentially causally related. For instance, a family of models has been discussed wherein jets or a wind can be launched vertically from a disk through a coupling between a spiral density wave in the disk and a Rossby vortex (Tagger & Pellat 1999; Varniere, Rodriguez, & Tagger 2002; Rodriguez, Varniere, Tagger, & Durouchoux 2002). It is possible, then, that the few $\times 100$ s variations seen in H 1743–322 are due to a density structure which acts to drive jets close to the black hole, and that the same wave modulates a disk wind far from the black hole. It is not yet clear if such a mechanism could be at work in driving both jets and a disk wind, but if so, then the appearance of ionized Fe absorption lines in strong jet sources like GRO J1655–40, GRS 1915+105, and now H 1743–322 would be explained naturally.

We note that using reduction methods exactly like those detailed for H 1743–322, we have detected Fe XXV and Fe XXVI lines in a 60 ksec *Chandra*/HETGS spectrum of Cygnus X-1

obtained on 3 March 2004, when the source was in a canonical low/hard state (Miller et al. 2004c, in prep.). Cygnus X-1 is known to produce a compact, steady radio jet in this state (Stirling et al. 2001). Highly ionized Fe absorption lines have also been detected in the neutron star system GX 13+1 (Sidoli et al. 2002). Interestingly, GX 13+1 is also a radio emitter in which a delay between its X-ray spectral hardness and radio brightness has been observed which is very similar to that seen in GRS 1915+105 (Homan et al. 2004a), strongly suggesting a compact jet is also at work in this system.

However, simultaneous radio observations of H 1743–322 with the VLA/VLBA reveal that the radio source was quite strong during the first and second *Chandra* observations — nearly 10 mJy at GHz frequencies) — but only 2 mJy during the third observation, and less than 1 mJy during the fourth observation (Rupen et al. 2004, in prep.). Thus, strong radio activity (indicative of a jet) is seen during the second *Chandra* observation (where absorption lines are not observed), and absorption lines are clearly observed in the third and fourth *Chandra* observations when the radio flux was low. At minimum, this suggests that if jets and ionized absorption are causally related, they are not related in a simple way. Both may merely be the effect of a strongly active corona, for instance.

Moreover, the detection of highly ionized Fe absorption lines in high inclination neutron star binaries may signify that it is unlikely that ionized absorption lines are tied to jet production through a mechanism like AEI. Similar lines have also been seen in the persistent emission of the (edge-on) dipping neutron star binaries X 1254–690 (Boirin & Parmar 2003), X 1624–490 (Parmar et al. 2002), MXB 1658–29 (Sidoli et

al. 2001) and 4U 1916–053 (Boirin et al. 2004). In contrast to the absorption lines in the black hole systems H 1743–322, GX 339–4, and XTE J1650–500, the absorption lines in these edge-on neutron star binaries are not significantly blue-shifted. Although the appearance of lines in both black hole and neutron star systems suggests a related physical origin, the lack of blue-shifts in the lines seen in neutron stars may hint at a different physical picture. Without significant blue-shifts, it is difficult to clearly tie the lines to an outflow. The lines may not be due to absorption in an outflow, but might be due to absorption in ambient gas within the system. The absorption lines in MXB 1658–29, for instance, are not observed to vary with orbital phase or even during dipping events (Sidoli et al. 2001), which suggests that the absorbing gas is not as close to the compact object as the absorbing gas in black hole systems.

We wish to thank CXC Director Harvey Tananbaum and the CXC staff, and Jean Swank and the *RXTE* staff, for making these TOO observations. We thank John Houck for assistance with ISIS. JMM acknowledges helpful discussions with Mike Nowak, David Huenemoerder, Aneta Siemiginowska, Rob Fender, Herman Marshall, and Patrick Wojdowski. JMM gratefully acknowledges support from the NSF through its Astronomy and Astrophysics Postdoctoral Fellowship program. WHGL and JH gratefully acknowledge support from NASA. DS acknowledges support from the SAO Clay Fellowship. This research has made use of the data and resources obtained through the HEASARC on-line service, provided by NASA-GSFC.

REFERENCES

- Abramowicz, W., & Kluzniak, W., 2003, in the proc. of the conference “X-ray Timing 2003”, Cambridge, MA, 3–5 Nov. 2003, astro-ph/0312396
- Arnaud, K. A., and Dorman, B., 2000, XSPEC is available via the HEASARC on-line service, provided by NASA/GSFC
- Ballantyne, D. R., Ross, R., & Fabian, A. C., 2001, MNRAS, 323, 506
- Boirin, L., & Parmar, A. N., 2003, A&A, 407, 1079
- Boirin, L., Parmar, A. N., Barret, D., Paltani, S., & Grindlay, J. E., 2004, A&A, 418, 1061
- Dickey, J. M., and Lockman, F. J., 1990, ARA&A, 28, 215
- Doxsey, R., et al., 1977, IAU Circ. 3113
- Elvis, M., 2000, ApJ, 545, 63
- Fender, R. P., Wu, K., Johnston, H., Tzioumis, T., Jonker, P., Spencer, R., & van der Klis, M., 2004, Nature, 427, 222
- Frank, J., King, A. R., & Raine, D., 2002, “Accretion Power in Astrophysics”, 3rd edition, Cambridge: Cambridge Univ. Press
- George, I. M., & Fabian, A. C., 1991, MNRAS, 249, 352
- Homan, J., Wijnands, R., van der Klis, M., Belloni, T., van Paradijs, J., Klein-Wolt, M., Fender, R., & Mendez, M., 2001, ApJS, 132, 377
- Homan, J., Miller, J. M., Wijnands, R., Steeghs, D., Belloni, T., van der Klis, M., & Lewin, W. H. G., 2003, ATEL 162
- Homan, J., et al., 2003b, ApJ, 586, 1262
- Homan, J., Wijnands, R., Rupen, M. P., Fender, R., Hjellming, R. M., di Salvo, T., & van der Klis, M., 2004, A&A, 418, 255
- Homan, J., et al., 2004b, ApJ, subm.
- Houck, J. C., & Denicola, L. A., 2000, Astronomical Data Analysis Software and Systems IX, in ASP Conference Proceedings, vol. 216, eds. N. Manset, C. Veillet, & D. Crabtree; ISIS is available at <http://space.mit.edu/CXC/ISIS>
- Kaluzienski, L. J., & Holt, S. S., 1977, IAU Circ. 3099
- Kotani, T., Ebisawa, K., Dotani, T., Inoue, H., Nagase, F., Tanaka, Y., & Ueda, Y., 2000, ApJ, 539, 413
- Kuulkers, E., Wijnands, R., Belloni, T., Mendez, M., van der Klis, M., & van Paradijs, J., 1998, ApJ, 497, 753
- Laor, A., 1991, ApJ, 376, 90
- Lee, J. C., Reynolds, C. S., Remillard, R. A., Schulz, N. S., Blackman, E. G., & Fabian, A. C., 2002, ApJ, 567, 1102
- Maloney, P. R., Begelman, M. C., & Pringle, J. E., 1996, ApJ, 472, 582
- Markwardt, C. B., & Swank, J. H., 2003a, ATEL 133
- Markwardt, C. B., & Swank, J. H., 2003b, ATEL 136
- McClintock, J. E., and Remillard, R. A., 2003, astro-ph/0306213, to appear in “Compact Stellar X-ray Sources”, Cambridge University Press, eds. W. H. G. Lewin and M. van der Klis
- Merloni, A., Fabian, A. C., & Ross, R. R., 2000, MNRAS, 313, 193
- Miller, M. C., 2003, in the proc. of the conference “X-ray Timing 2003”, Cambridge, MA, 3–5 Nov. 2003, astro-ph/0312449
- Miller, J. M., et al., 2001, ApJ, 563, 928
- Miller, J. M., et al., 2004, ApJ, 601, 450
- Miller, J. M., Raymond, J., Fabian, A. C., Wijnands, R., van der Klis, M., & Lewin, W. H. G., 2004b, ATEL 221
- Mitsuda, K., et al., 1984, PASJ, 36, 741
- Morales, R., & Fabian, A. C., 2002, MNRAS, 329, 209
- Murray, N., & Chiang, J., 1997, ApJ, 474, 91
- Parmar, A. N., Oosterbroek, T., Boirin, L., & Lumb, D., 2002, A&A, 386, 910
- Petrucchi, P. O., Merloni, A., Fabian, A., Haardt, F., & Gallo, E., 2001, MNRAS, 328, 501
- Proga, D., 2003, ApJ, 585, 406
- Raymond, J. C., 1993, ApJ, 412, 267
- Remillard, R. A., Munro, M. P., McClintock, J. E., & Orosz, J. A., 2002, ApJ, 580, 1030
- Revnivtsev, M., et al., 2003, ATEL 132
- Reynolds, C. S., 1997, MNRAS, 286, 513
- Rodriguez, J., Varniere, P., Tagger, M., & Durouchoux, Ph., 2002, A&A, 387, 487
- Ross, R. R., Fabian, A. C., & Young, A. J., 1999, MNRAS, 306, 461
- Rupen, M. R., Mioduszewski, A., & Dhawan, V., 2003, ATEL 139
- Rupen, M. R., Mioduszewski, A., & Dhawan, V., 2004, BAAS, 36, 2, 5.16
- Shimura, T., and Takahara, F., 1995, ApJ, 445, 780
- Sidoli, L., Oosterbroek, T., Parmar, A. N., Lumb, D., & Erd, C., 2001, A&A, 379, 540
- Sidoli, L., Parmar, A. N., Oosterbroek, T., & Lumb, D., 2002, A&A, 385, 940
- Spitzer, L., 1978, in “Physical Processes in the Interstellar Medium”, Wiley-Interscience, New York
- Steeghs, D., Miller, J. M., Kaplan, D., & Rupen, R., 2003, ATEL 146
- Stirling, A. M., Spencer, R. E., de la Force, C. J., Garret, M. A., Fender, R. P., & Ogley, R. N., 2001, MNRAS, 327, 1273
- Strohmayer, T., 2001a, ApJ, 552, L49
- Strohmayer, T., 2001b, ApJ, 554, L169
- Tagger, M., & Pellat, R., 1999, A&A, 349, 1003
- Titarchuk, L., 1994, ApJ, 434, 570

Ueda, Y., Inoue, H., Tanaka, Y., Ebisawa, K., Nagase, F., Kotani, T., & Gehrels, N., 1998, *ApJ*, 492, 782
Varniere, P., Rodriguez, J., & Tagger, M., 2002, *A&A*, 387, 497

Verner, D. A., Verner, E. M., & Ferland, G. J., 1996, *ADNDT*, 64, 1
White, N. E., & Marshall, F. E., 1984, *ApJ*, 281, 354
Zdziarski, A. A., Lubinski, P., Gilfanov, M., & Revnitsev, M., 2003, *MNRAS*, 342, 355

TABLE 1

Observation Log

Instrument	Start Time	Net Exposure (ksec)
CXO/ACIS+HETGS	2003-05-01T21:41:03	48.8
RXTE/PCA 1a	2003-05-01T17:00:32	25.2
RXTE/PCA 1b	2003-05-02T00:02:24	0.8
RXTE/PCA 1c	2003-05-02T00:54:08	3.3
CXO/ACIS+HETGS	2003-05-28T04:09:21	45.5
RXTE/PCA 2a	2003-05-28T05:28:48	1.5
RXTE/PCA 2b	2003-05-28T06:44:16	16.1
RXTE/PCA 2c	2003-05-28T14:28:32	5.6
CXO/ACIS+HETGS	2003-06-23T15:56:10	50.0
RXTE/PCA 3	2003-06-23T17:05:20	13.3
CXO/ACIS+HETGS	2003-07-30T15:57:58	50.2
RXTE/PCA 4a	2003-07-30T19:48:48	0.6
RXTE/PCA 4b	2003-07-30T21:22:40	0.6
RXTE/PCA 4c	2003-07-31T00:32:48	0.6

NOTE.—The *Chandra* and *RXTE* observations discussed in this work are tabulated above. The start time is given in “TT” units. The net exposure is the exposure after standard *Chandra* and *RXTE* filtering has been applied.

TABLE 2

Continuum X-ray Spectral Fit Parameters

Observation	1a	1b	1c	2a	2b	2c	3	4
N_H (10^{22})	2.3	2.3	2.3	2.3	2.3	2.3	2.3	2.3
kT (keV)	1.22(1)	1.22(1)	1.21(2)	1.21(2)	1.23(1)	1.24(1)	1.09(1)	1.009(3)
K_{MCD} (10^3)	0.58(1)	0.88(4)	0.95(4)	0.69(4)	0.62(3)	0.64(3)	1.11(3)	1.01(2)
Γ	2.39(3)	2.4(1)	2.6(1)	2.61(4)	2.63(3)	2.64(2)	2.11(4)	3.3(3)
K_{pl}	1.7(1)	2.0(6)	3.0(6)	9(1)	13.3(6)	14.8(8)	0.63(6)	$1.3^{+0.9}_{-0.6}$
F_{3-100} (10^{-8})	1.4(2)	1.9(7)	1.9(5)	2.2(4)	2.6(2)	2.8(3)	1.3(2)	0.6(4)
f_{hard} (3-100)	0.21	0.21	0.21	0.50	0.58	0.57	0.23	0.06
L_X (3-100) (10^{38} erg/s)	1.2(2)	1.7(7)	1.7(4)	1.9(3)	2.3(2)	2.4(2)	1.1(2)	0.5(3)
$F_{0.5-10}$ (10^{-8})	3.2(5)	5(2)	5(1)	6(1)	7.0(7)	7.8(8)	3.3(4)	2(1)
f_{hard} (0.5-10)	0.19	0.15	0.14	0.52	0.62	0.63	0.09	0.17
L_X (0.5-10) (10^{38} erg/s)	2.8(4)	4(2)	4(1)	5(1)	6.1(6)	6.8(7)	2.9(3)	2(1)
χ^2/ν	78.8/74	97.0/74	98.9/74	89.5/74	90.2/74	94.2/74	117.9/74	245.1/228
Fe K α (FWHM=0 keV) (eV)	< 4	< 4	< 3	< 7	< 9	< 12	< 12	< 6
Fe K α (FWHM=2 keV) (eV)	< 6	< 7	< 7	< 14	< 15	< 20	< 44	< 9

NOTE.—The results of spectral fits to the *RXTE* PCU-2 and HEXTE-A spectra in the 3–100 keV band are presented above. The observation numbers correspond to those in Table 1. As observations coinciding with the fourth *Chandra* spectrum are disk-dominated and show little variability, they were fit jointly. Individual fits revealed that N_H was consistent with 2.3×10^{22} cm $^{-2}$ for each observation, and was therefore fixed in the fits reported here. The normalization of the power-law component is photons cm $^{-2}$ s $^{-1}$ keV $^{-1}$ at 1 keV. The fluxes quoted above are “unabsorbed” fluxes. The distance to H 1743–322 is unknown; a Galactic Center distance of $d = 8.5$ kpc was assumed to calculate each luminosity value. All errors are 90% confidence errors. The 95% confidence upper-limit on the equivalent width of narrow and broad Fe K α emission lines is quoted at the bottom of the table.

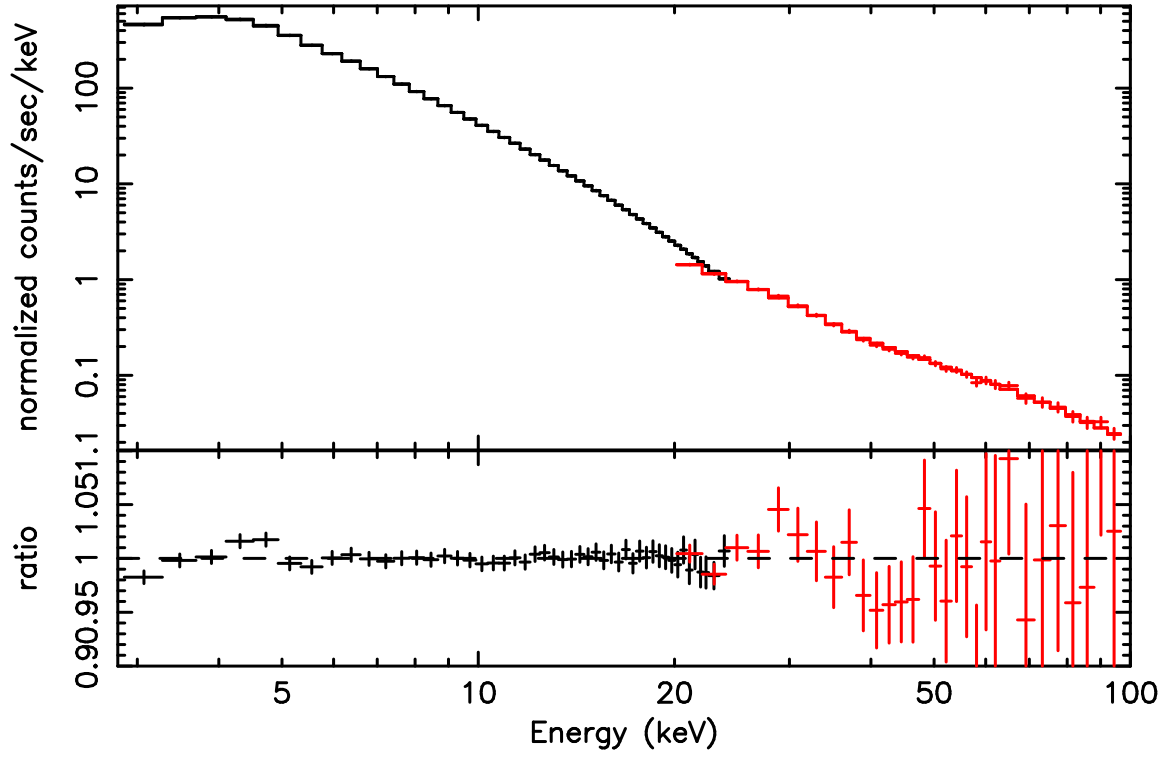


FIG. 1.— The *RXTE* spectrum of H 1743–322 from observation 2b is shown above, fitted with a multicolor disk blackbody plus power-law continuum model (see Table 2). The spectrum is remarkably featureless, with no evidence for disk reflection features. Given the high-frequency (240 Hz) QPOs were detected in this data — indicating the disk is likely very close to the assumed black hole — we might have expected to see strongly skewed disk reflection features.

Ionized Absorption in H 1743–322

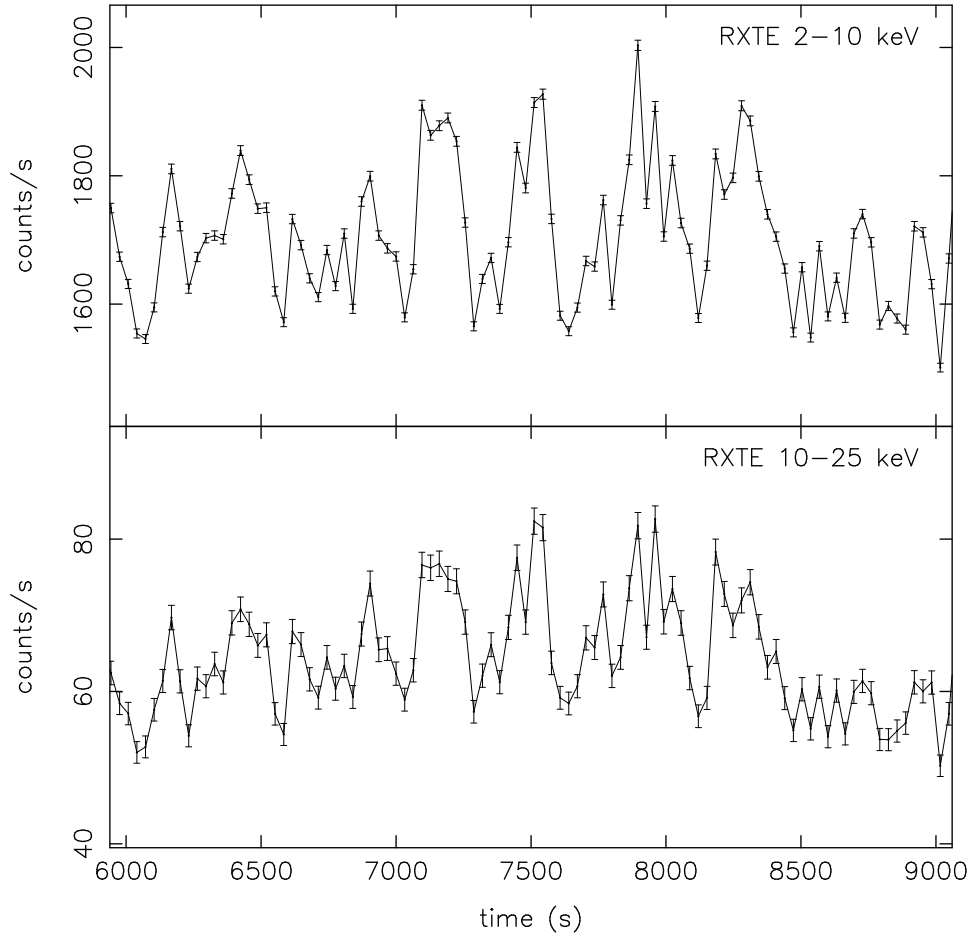


FIG. 2.— Lightcurves from the *RXTE* observation 1b are shown above. The data have been binned into 32 s bins. The variability seen on *few* \times 100s timescales is very similar to that seen in the *Chandra* lightcurves (see Figure 5).

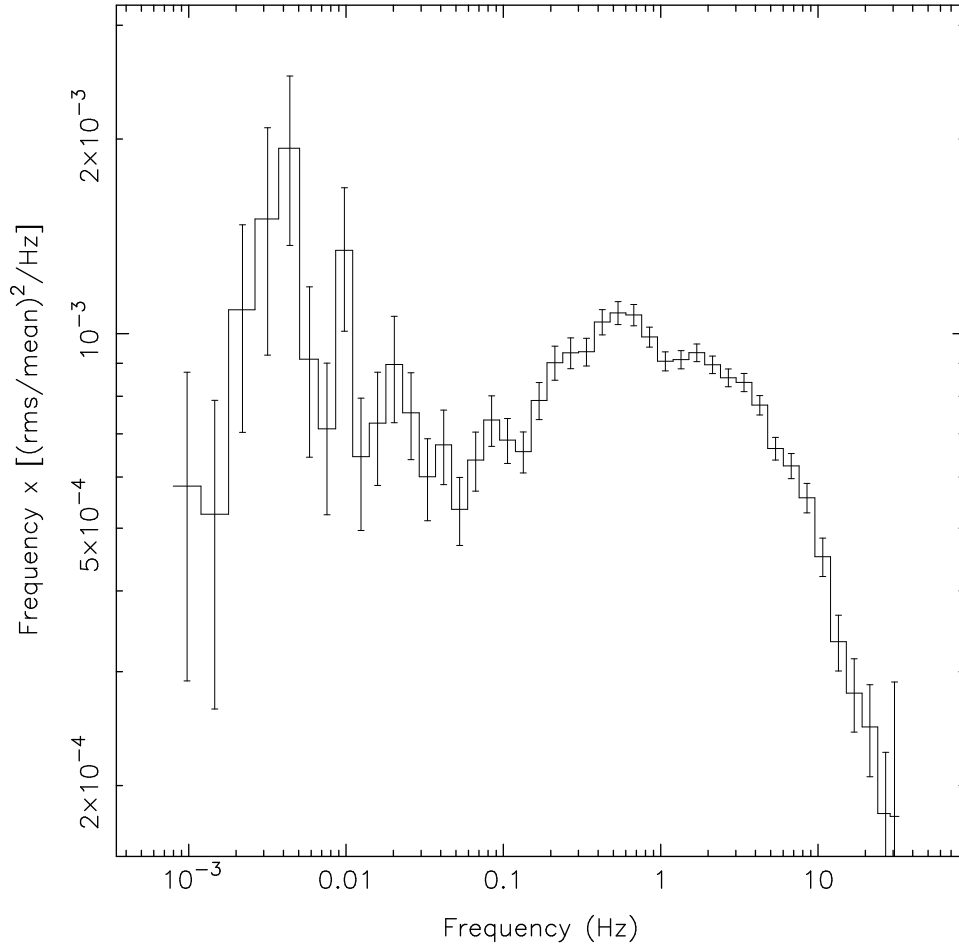


FIG. 3.— The 2–60 keV power density spectrum of *RXTE* observation 1a is shown above. The Poisson level has been subtracted. The broad feature at approximately 4×10^{-3} Hz corresponds to the variability seen in the lightcurve shown in Figure 2; this feature can be fit with a Lorentzian.

TABLE 3

X-ray Absorption Lines in the Spectra of H 1743–322

Obs.	Ion	Theor. (Å)	Meas. (Å)	Shift (km/s)	FWHM (10 ⁻³ Å)	FWHM (km/s)	Flux (10 ⁻³ ph/cm ² /s)	W (mÅ)	N _Z (10 ¹⁷ cm ⁻²)	N _H (10 ²² cm ⁻²)
1	Fe XXV	1.850	1.848(1)	-320 ± 160	0.7 ^{+4.7} _{-0.4}	110 ⁺⁷⁴⁰ ₋₆₀	0.48(8)	1.5(2)	0.62(8)	0.18(2)
1	Fe XXVI	1.780	1.776(1)	-670 ± 170	10.6 ± 2.4	1800 ± 400	1.4(1)	5.1(5)	4.4(4)	1.3(1)
2	Fe XXV	1.850	—	—	—	—	< 0.5	< 1.2	< 0.5	< 0.2
2	Fe XXVI	1.780	—	—	—	—	< 0.3	< 0.9	< 0.8	< 0.2
3	Fe XXV	1.850	1.851(2)	+160 ± 320	2.8 ^{+6.8} _{-2.8}	450 ⁺¹¹⁰⁰ ₋₄₅₀	0.25(7)	1.4(4)	0.6(2)	0.18(6)
3	Fe XXVI	1.780	1.778(1)	-340 ± 170	6.1 ^{+4.5} _{-6.1}	1030 ⁺⁷⁴⁰ ₋₁₀₃₀	0.53(8)	3.5(5)	3.0(4)	0.9(1)
4	Fe XXV	1.850	1.850(1)	0 ± 160	0.9 ^{+3.3} _{-0.9}	150 ⁺⁵⁵⁰ ₋₁₅₀	0.43(4)	4.3(4)	1.8(2)	0.55(6)
4	Fe XXVI	1.780	1.781(1)	+170 ± 170	11.3 ± 3.1	1900 ± 500	0.54(7)	6.4(8)	5.5(7)	1.7(1)

NOTE.—Fit parameters for the He-like Fe XXV (1s²–1s2p) and H-like Fe XXVI (1s–2p) resonance absorption lines detected in the combined first-order *Chandra*/HEG spectra of H 1743–322. The errors on all line fit parameters are 1σ confidence errors. Errors quoted in parentheses are symmetric errors in the last digit. Positive velocity shifts correspond to red-shifts and negative velocity shifts correspond to blue-shifts. Significant lines were not detected in observation 2; 95% confidence upper-limits are reported assuming the same line centroid and FWHM values as measured in observation 1. Only the Fe XXVI lines in observations 1 and 4 are resolved. Equivalent neutral hydrogen column densities were calculated assuming an Fe abundance of 3.3×10^{-5} relative to hydrogen. Line wavelengths and oscillator strengths are taken from Verner et al. (1996b).

TABLE 4

X-ray Absorption Lines in Count-rate-selected Spectra of H 1743–322

Obs.	Ion	Theor. (Å)	Meas. (Å)	Shift (km/s)	FWHM (10 ⁻³ Å)	FWHM (km/s)	Flux (10 ⁻³ ph/cm ² /s)	W (mÅ)	N _Z (10 ¹⁷ cm ⁻²)	N _H (10 ²² cm ⁻²)
1 (>mean)	Fe XXV	1.850	—	—	< 10	< 1600	< 0.6	< 1.8	< 0.8	< 0.2
1 (<mean)	Fe XXV	1.850	1.848(1)	-320 ± 160	< 10	< 1600	0.6(1)	1.9(3)	0.8(1)	0.24(4)
1 (>mean)	Fe XXVI	1.780	1.776(1)	-670 ± 170	11.8 ± 4.7	2000 ± 700	1.3(2)	4.3(7)	3.7(6)	1.1(2)
1 (<mean)	Fe XXVI	1.780	1.776(1)	-670 ± 170	10 ⁺¹ ₋₂	1700 ⁺²⁰⁰ ₋₄₀₀	1.4(2)	5(1)	4(1)	1.3(3)
1 (mean+5 c/s)	Fe XXV	1.850	—	—	< 10	< 1600	< 0.8	< 0.24	< 1	< 0.3
1 (mean-5 c/s)	Fe XXV	1.850	1.849(1)	-160 ± 160	< 10	< 1600	0.9(1)	2.8(3)	1.2(1)	0.36(4)
1 (mean+5 c/s)	Fe XXVI	1.780	1.775(1)	-840 ± 170	11.8 ± 4.7	2000 ± 700	1.4(2)	4.6(7)	3.9(6)	1.2(2)
1 (mean-5 c/s)	Fe XXVI	1.780	1.777(1)	-510 ± 170	14 ± 5	2400 ± 900	1.5(2)	5(1)	4(1)	1.3(3)
3 (norm.)	Fe XXV	1.850	—	—	< 10	< 1600	< 0.3	< 1.5	< 0.6	< 0.2
3 (dip)	Fe XXV	1.850	1.850(1)	0 ± 160	< 10	< 1600	0.7(1)	4.3(6)	1.5(2)	0.45(7)
3 (norm.)	Fe XXVI	1.780	1.777(1)	-510 ± 170	< 10	< 1600	0.5(1)	3.1(6)	2.1(5)	0.6(2)
3 (dip)	Fe XXVI	1.780	1.778(1)	-340 ± 170	< 10	< 1600	0.6(1)	4.4(7)	3.8(6)	1.2(2)

NOTE.—Fit parameters for the He-like Fe XXV (1s²–1s2p) and H-like Fe XXVI (1s–2p) resonance absorption lines detected in the combined first-order count-rate selected *Chandra*/HEG spectra of H 1743–322. The errors on all line fit parameters are 1σ confidence errors. Errors quoted in parentheses are symmetric errors in the last digit. Where lines are not detected, 95% confidence upper limits are given. Where measurements are not reported, they are fixed to those measured in the time-averaged spectra (see Table 3). Positive velocity shifts correspond to red-shifts and negative velocity shifts correspond to blue-shifts. Equivalent neutral hydrogen column densities were calculated assuming an Fe abundance of 3.3×10^{-5} relative to hydrogen. Line wavelengths and oscillator strengths are taken from Verner et al. (1996b).

TABLE 5

Absorbing Plasma Parameters

Observation	n_{rmax} (cm ⁻³)	r_{min} (cm)	r_{max} (cm)	N (cm ⁻²)	\dot{M}_{300} (g s ⁻¹)
1	1.1×10^{12}	1.2×10^9	4.0×10^{10}	4.4×10^{22}	1.3×10^{18}
2	$< 1.2 \times 10^{10}$	—	4.0×10^{11}	$< 5.3 \times 10^{21}$	—
3	2.2×10^{11}	1.5×10^9	1.0×10^{11}	2.2×10^{22}	1.7×10^{18}
4	1.8×10^{11}	3.2×10^7	1.3×10^9	3.7×10^{22}	2.1×10^{14}

NOTE.—Parameters for the absorbing plasma model discussed in the text are given here. A single-zone absorbing medium in photoionization equilibrium is assumed by the model. The parameter \dot{M}_{300} refers to the mass outflow rate assuming a velocity of 300 km/s. The parameter n_{rmax} is the density at r_{max} .

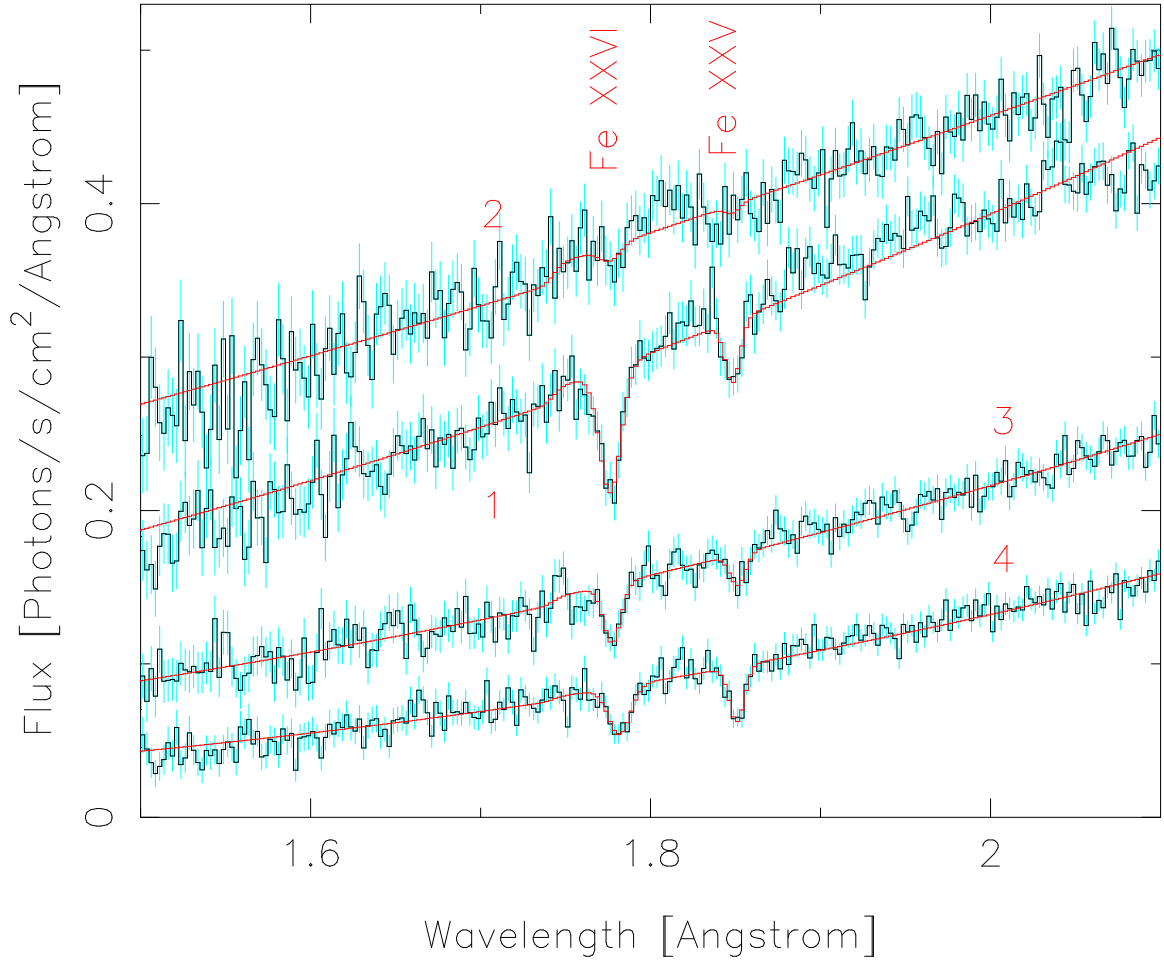


FIG. 4.— Variable He-like Fe XXV ($\lambda = 1.850 \text{ \AA}$) and H-like Fe XXVI ($\lambda = 1.780 \text{ \AA}$) absorption lines in the combined time-averaged first-order *Chandra*/HEG spectra of H 1743–322 are shown above. The spectra are numbered in order of observation. The data are plotted in black, 1σ error bars are plotted in blue, and the model for each spectrum is plotted in red. The continuum models consist of phenomenological power-law components with Galactic absorption to supply the appropriate neutral Fe K edges from the ISM. The absorption lines were modeled using simple Gaussian components. There is no significant absorption in the spectra from observation 2.

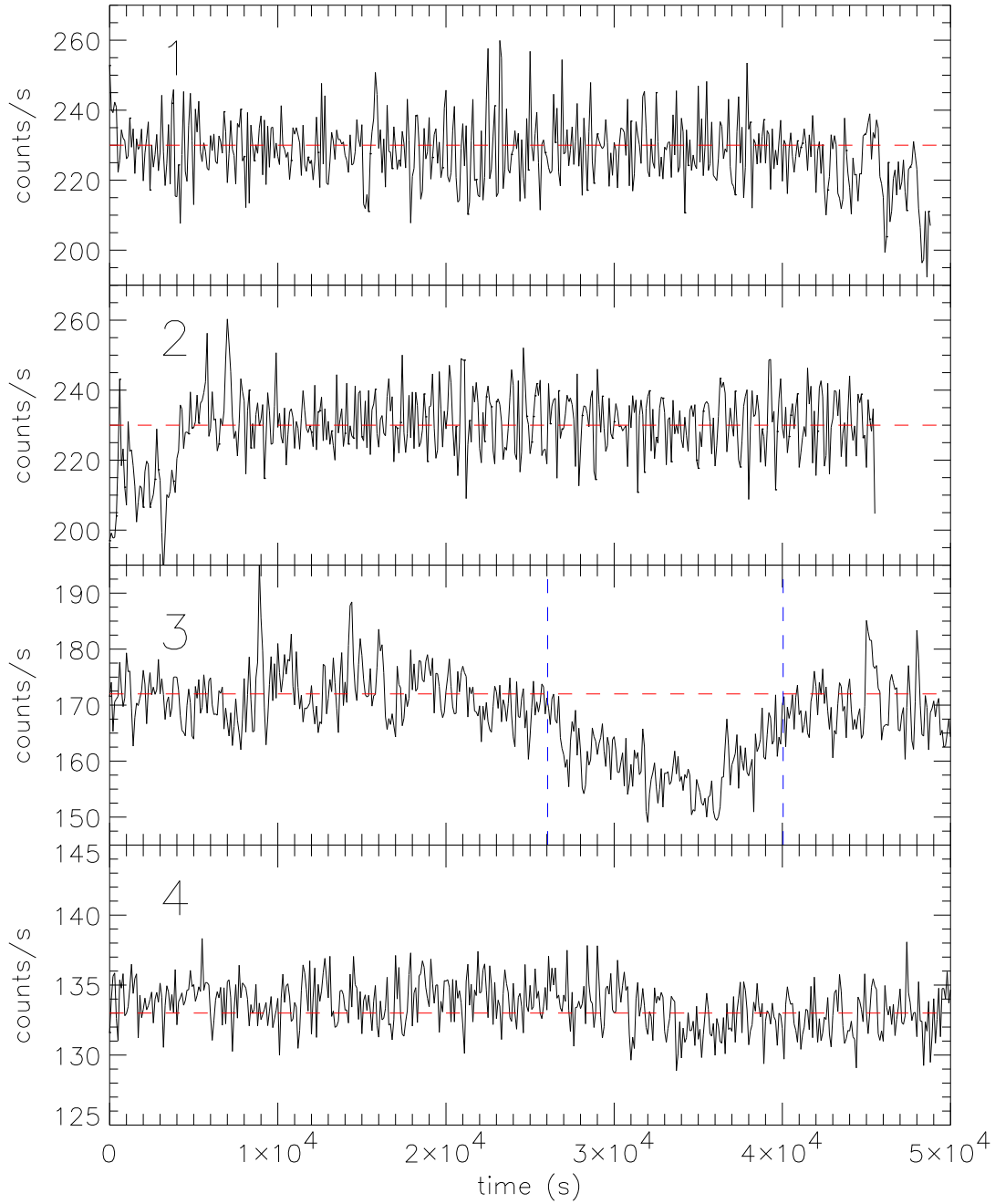


FIG. 5.— The 0.5–10.0 keV lightcurves of *Chandra* observations 1–4 are shown above. The data were rebinned to have bin lengths of 100 seconds. The mean 1σ error in each bin above is less than 1.5 counts/s; the extreme variability observed is indeed real. The mean count rate in each observation (excluding the dip in observation 3, marked with vertical blue lines) is shown with a horizontal red line. The ~ 14 ksec dip seen in observation 3 indicates that H 1743–322 is likely viewed at a high inclination; weaker dips may be seen at the end of observation 1 and the start of observation 2.

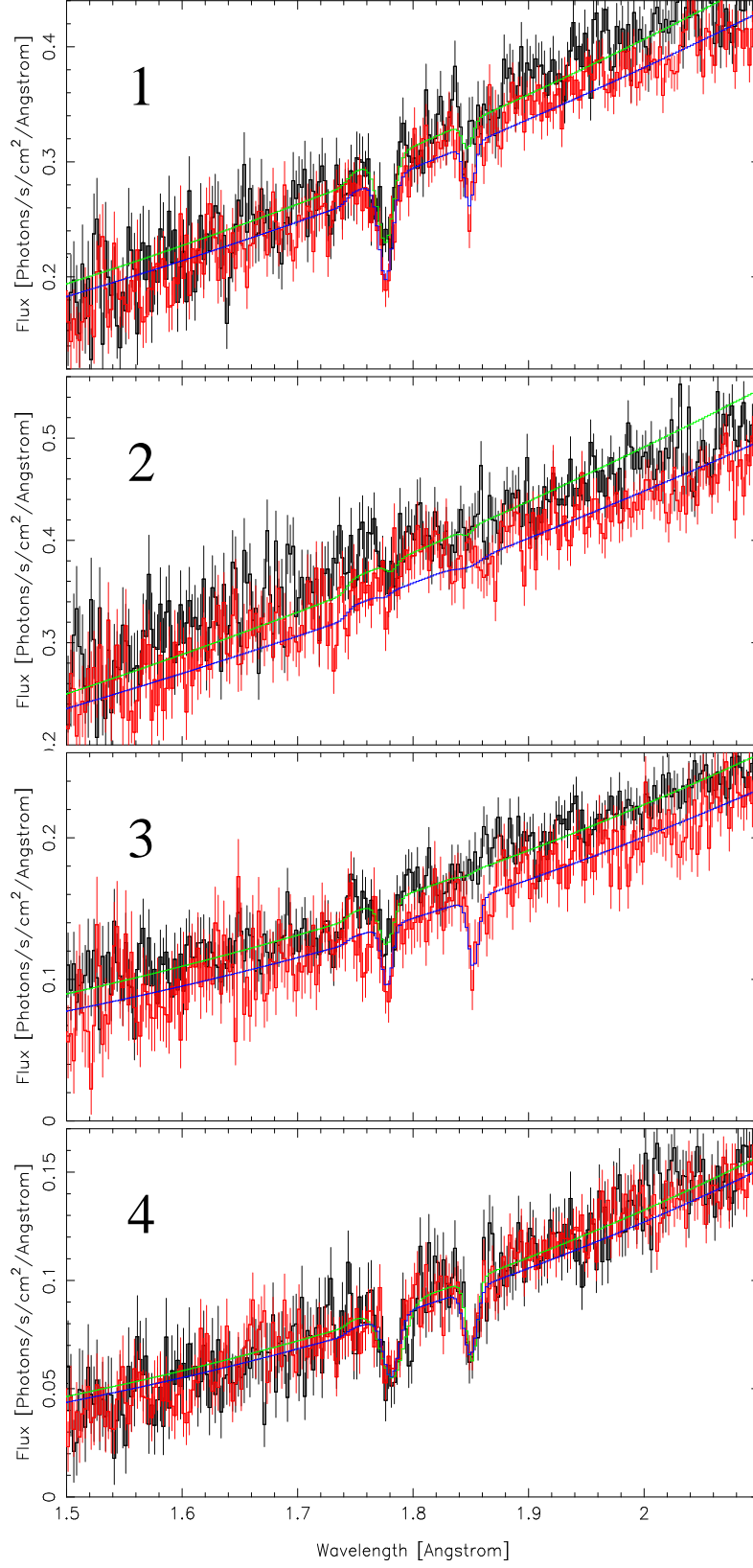


FIG. 6.— Count-rate-selected *Chandra*/HETGS spectra from observations 1–4 are shown above. In observations 1, 2, and 4, the black data corresponds to periods above the mean count rate, and the red data corresponds to periods below the mean count rate. The best-fit model for the black data is shown in green, and the best-fit model for the red data is shown in blue. In observation 1, there is evidence that the Fe XXV ($\lambda = 1.850$ Å) and Fe XXVI ($\lambda = 1.780$ Å) absorption lines are stronger at low count rates. The black data from observation 3 corresponds to the spectrum prior to the ~ 14 ksec dip seen in Fig. 5, and the red data correspond to the spectrum within the dip. The Fe XXV absorption line is clearly stronger within the dip.

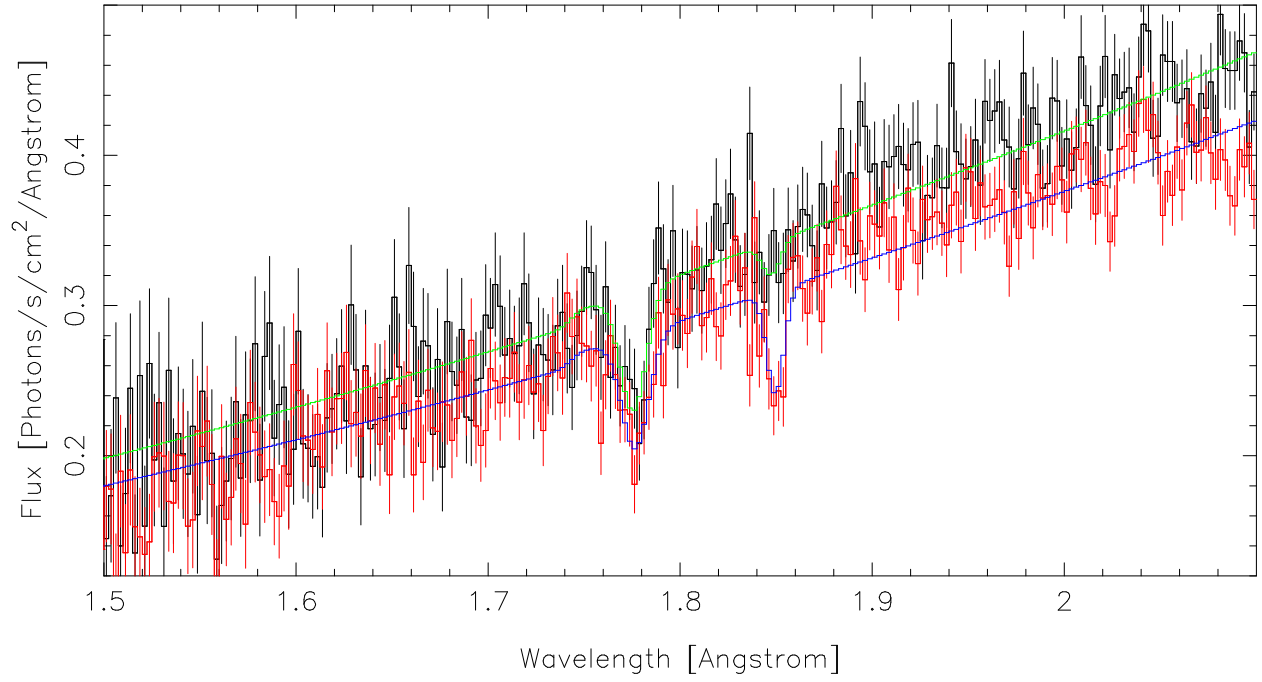


FIG. 7.— Count-rate selected spectra from Chandra observation 1 are shown above. The spectrum in black was taken from time intervals with count rates greater than the mean plus 5.0 counts/sec, while the spectrum in red was taken from time intervals with count rates less than the mean minus 5.0 counts/sec. These spectra show a more distinct change in the depth of the Fe XXV line than those shown in panel 1 of Fig. 6.